# Artemin Crystal Structure Reveals Insights into Heparan Sulfate Binding‡

Laura Silvian,* Ping Jin, Paul Carmillo, P. Ann Boriack-Sjodin, Carolyn Pelletier, Mia Rushe,^ BangJian Gong, Dinah Sah,|| Blake Pepinsky, and Anthony Rossomando

*Department of Drug Discovery, Biogen Idec, Inc., 12 Cambridge Center, Cambridge, Massachusetts 02142*

*Received January 6, 2006; Revised Manuscript Received March 31, 2006*

ABSTRACT: Artemin (ART) promotes the growth of developing peripheral neurons by signaling through a multicomponent receptor complex comprised of a transmembrane tyrosine kinase receptor (cRET) and a specific glycosylphosphatidylinositol-linked co-receptor (GFRα3). Glial cell line-derived neurotrophic factor (GDNF) signals through a similar ternary complex but requires heparan sulfate proteoglycans (HSPGs) for full activity. HSPG has not been demonstrated as a requirement for ART signaling. We crystallized ART in the presence of sulfate and solved its structure by isomorphous replacement. The structure reveals ordered sulfate anions bound to arginine residues in the pre-helix and amino-terminal regions that were organized in a triad arrangement characteristic of heparan sulfate. Three residues in the pre-helix were singly or triply substituted with glutamic acid, and the resulting proteins were shown to have reduced heparin-binding affinity that is partly reflected in their ability to activate cRET. This study suggests that ART binds HSPGs and identifies residues that may be involved in HSPG binding.

The glial cell line-derived neurotrophic factor (GDNF)[1] family of ligands (GFLs) are neurotrophic growth factors that promote the survival of distinct populations of central and peripheral neurons. Four GFLs have been described to date: artemin [ART (*1*), also known as neublastin (*2*) and enovin (*3*)], neurturin [NTN (*4*)], persephin [PSP (*5*)], and GDNF (*6*). ART exhibits a restricted pattern of expression in the developing vasculature and sclerotomes (*7*), whereas GDNF is expressed in multiple tissues during development and in adulthood (*8*).

GFLs are biologically active covalently linked homodimers, in which each monomer has a "cystine knot" topology. This cystine knot was identified first through the structure of transforming growth factor β2 [TGF-β2 (*9*, *10*)] and can be recognized from the primary sequence by a characteristic cysteine-spacing motif. These proteins contain two antiparallel β strands ("fingers"), which are linked by the cystine knot. In the TGF-β superfamily of cystine-knot proteins, including osteogenic protein 1 [OP-1 or BMP7 (*11*)], bone morphogenic protein 2 [BMP-2 (*12*)], and GDNF, the dimer arrangement is antiparallel and includes an interchain disulfide bond. A helix is inserted in the loop between the two fingers, termed the "wrist", and packs against the flat fingers of the other monomer in a "handshake" arrangement. Other cystine-knot proteins differ from the TGF-β family; they do not contain a helical "wrist", and their dimerization interfaces are different. These structures include platelet-derived growth factor [PDGF (*13*)], nerve growth factor [NGF (*14*)], and vascular endothelial growth factor [VEGF (*15*)], among others. Of the GFLs, GDNF is the only family member whose crystal structure has been solved [PDB ID 1AGQ; *16*]. The GDNF crystal contains two covalent homodimers in its asymmetric unit. The two GDNF homodimers differ in the relative hinge angle between the "finger-tips" and "wrist" within their respective monomers.

The homodimeric GFLs can activate cRET tyrosine kinase by forming a complex containing the cRET tyrosine kinase receptor and a preferred high-affinity GPI-linked co-receptor (GFRα) in a proposed stoichiometry of GFL homodimer−$GFR\alpha_2$−$RET_2$ (*17*). Four GFRα co-receptors have been identified (GFRα1−4) (*18*−*21*). Each preferentially binds to one of the four GFLs; however, crossover may occur in some instances (*22*). ART interacts selectively with the co-receptor GFRα3, whereas GDNF interacts selectively with GFRα1 (*1*, *17*, *23*).

A variety of experiments suggest that the finger loops of GFLs interact directly with their respective GFRα co-receptors. On the basis of mutagenesis experiments, GFRα1 was shown to bind the acidic and hydrophobic finger loops of GDNF (*24*). In a domain-swapping experiment between GFLs, the preference of ART for co-receptor GFRα3 was ascribed to the specific sequences in the pre-helix region of the wrist and the β strands of finger 2 (*22*). In support of the finger loops being essential, a recent model of the

‡ Coordinates and structure factors have been deposited in the Protein Data Bank with PDB ID 2ASK.

* To whom correspondence should be addressed. Telephone: (617) 679-2208. Fax: (617) 679-2616. E-mail: laura.silvian@biogenidec.com.

^ New address: Research, Novartis Institutes for Biomedical Research Inc., 250 Mass Ave., Cambridge, MA 02139.

|| New address: Alnylam Pharmaceuticals, Inc., 300 Third St., Cambridge, MA 02142.

[1] Abbreviations: GDNF, glial cell line-derived neurotrophic factor; GFL, GDNF family of ligands; ART, artemin; ART113, full-length human artemin with 113 amino acids; NTN, neurturin; PSP, persephin; TGF-β2, transforming growth factor β2; OP-1, osteogenic protein 1; BMP-2, bone morphogenic protein 2; PDGF, platelet-derived growth factor; NGF, nerve growth factor; VEGF, vascular endothelial growth factor; GFR-α, GPI-linked co-receptor; HSPG, heparan sulfate proteoglycan; GAG, glycosaminoglycan; HGF/SF, hepatocyte growth factor/scatter factor; FGF-1, fibroblast growth factor 1; bFGF, basic fibroblast growth factor; EGF, epidermal growth factor; KIRA, kinase receptor activation enzyme-linked immunosorbent assay.

10.1021/bi060035x CCC: $33.50 © 2006 American Chemical Society
Published on Web 05/13/2006

GFRα1/GDNF binding surface has been proposed that incorporates mutagenesis data and places essential arginines in proximity to acidic residues in the finger loops of GDNF (*25*).

The ability of many cytokines to promote receptor dimerization and signaling is often facilitated by membrane-bound heparan sulfate proteoglycans (HSPGs). Heparan sulfate is localized on cell surfaces and the extracellular matrix and is synthesized as a proteoglycan composed of a protein core and multiple glycosaminoglycan (GAG) chains. Heparin, in contrast, is a densely sulfonated glycosaminoglycan that resembles the GAG chains of the heparan sulfate proteoglycan (*26*) and is often used in in vitro studies. In previous studies, interactions between fibroblast growth factor 1 (FGF-1) and hepatocyte growth factor/scatter factor (HGF/SF) with their tyrosine kinase receptors FGFR2 and c-Met, respectively, were shown to be facilitated by GAGs (*27*, *28*). Recent studies have indicated that GDNF signaling is mediated by heparan sulfate. In one study, the phosphorylation state of cRET was altered after either heparinase III treatment or the addition of exogenous heparin, suggesting that GAGs mediate a direct interaction between GDNF and its receptors (*29*). More specifically, the 2-O sulfate moieties are required (*30*). Other studies have reported that GDNF-induced upregulation of the tyrosine-hydroxylase gene mRNA was enhanced by the addition of heparin (*31*). Therefore, it is of interest to determine whether the interactions of other members of the GDNF family with their receptors might also involve GAGs.

We present here the crystal structure of human ART and compare it to the previously solved GDNF structure. The ART structure contains three sulfate anions that are arranged in a triad motif and are suggestive of a GAG-binding site. On the basis of this structure, we generated four ART variants in which arginine residues that bind these sulfates were singly or triply substituted with glutamate and assayed for heparin-binding and heparin-dependent stimulation of signaling activity. These data identify a heparin-binding site on the ART surface that is distinct from the receptor-binding region.

## EXPERIMENTAL PROCEDURES

*Protein Expression and Crystallization.* ART and selenomethionine−ART were expressed in *Escherichia coli* as His-tagged fusion proteins with a Lysyl-endoprotease cleavage site immediately adjacent to the start of the mature 113 amino acid sequence. Selenomethionine-labeled ART was expressed in a methionine auxotrophic host using a standard procedure in which the methionine in minimal media was substituted with selenomethionine (*32*).

*E. coli* host BL21(DE3) plysS expressing either wild-type ART or mutant ART, or a selenomethionine auxotrophic host B834 (Novagen) expressing selenomethionine-incorporated ART were lysed in phosphate-buffered saline (5 mM $NaPO_4$, 150 mM NaCl, pH 6.5) using a Gaulin press. The folding procedures for mutant and selenomethionine-incorporated ART were essentially the same as wild-type ART given below but performed on a 1/20th scale. After centrifugation (30 min at 10 000 rpm) to isolate inclusion bodies, the pellets were washed 2 times with 20× volumes buffer [0.02 M Tris-HCl at pH 8.5 and 0.5 mM ethylenediaminetetraacetic acid (EDTA)] and then washed 2 times with the same buffer containing Triton X-100 (2%, v/v) followed by two additional buffer washes without detergent. The final pellets were suspended in 50 mL 6 M guanidine hydrochloride, 0.1 M Tris-HCl at pH 8.5, 0.1 M dithiothreitol (DTT), and 1 mM EDTA and homogenized using a polytron homogenizer followed by overnight stirring at room temperature. The solubilized proteins were clarified by centrifugation prior to denaturing chromatography through 5.5 L of Superdex 200 preparative resin (Amersham Biosciences) equilibrated with 0.05 M glycine/$H_3PO_4$ at pH 8.0 and eluted with 2 M guanidine-HCl at 20 mL/min.

Fractions containing ART were pooled and concentrated approximately 5-fold to 250 mL using an Amicon 2.5-L stirred cell concentrator. After filtration to remove any precipitate, the concentrated protein was subjected to renaturing sizing chromatography through Superdex 200 equilibrated with 0.1 M Tris-HCl at pH 7.8, 0.5 M guanidine-HCl, 8.8 mM reduced glutathione, and 0.22 mM oxidized glutathione. The column was run using 0.5 M guanidine-HCl at 20 mL/min. Fractions containing renatured ART were identified by sodium dodecyl sulfate−polyacrylamide gel electrophoresis (SDS−PAGE) to determine the presence of the dimeric product under nonreducing conditions, pooled, and stored at 4 °C for further processing.

The N-terminal histidine tag was removed enzymatically with lysyl-endopeptidase to produce 113 amino acid ART (ART113) or with trypsin to produce the 104 amino acid form (ART104). The protein sample was made with 0.1 M sodium chloride, 25 mM *N*-2-hydroxyethylpiperazine-*N*′-2-ethanesulfonic acid (HEPES) at pH 8.0, and 0.15 M guanidine-HCl and lysyl-endopeptidase (WAKO) added at a 1:600 (w/w) ratio of protease/ART. To generate ART104, trypsin (1:2000, w/w) was substituted for lysyl-endopeptidase using the same buffer. The samples were stirred at room temperature for 2 h, and the digest was subjected to Ni−NTA chromatography (Qiagen). The flow through from this chromatography step was subjected to further purification using SP−Sepharose (Amersham Biosciences). Eluted ART was aliquoted and stored at −70 °C.

For crystallization, ART113 was concentrated to 17 mg/mL in 0.8 M arginine. Crystals were grown with the hanging-drop vapor diffusion method using a sparce-matrix condition made of 1.25 M magnesium sulfate and 0.1 M 2-(*N*-morpholino)ethanesulfonic acid (MES) at pH 6.5 and 20 °C. The most reproducible crystals were obtained by microseeding. The crystals were cryoprotected by the addition of increasing amounts of ethylene glycol to the well solution in intervals of 5% every minute to a final concentration of 1.25 M magnesium sulfate, 0.1 M MES at pH 6.5, and 30% (v/v) ethylene glycol and then frozen by quick transfer into liquid nitrogen.

*Data Collection and Structure Determination and Refinement.* Crystals approximately 100 μm on each side frozen at −180 °C diffracted to 1.55 Å at beamline X4A at the National Synchrotron Light Source (Upton, NY). Data processing with the HKL program package (*33*) revealed the crystals belong to a *C*2 space group with one covalent dimer per asymmetric unit and approximate cell dimensions $a = 115$, $b = 34$, and $c = 56$ Å and $\alpha = \gamma = 90°$ and $\beta = 99°$.

The crystal structure was solved by combining multiple isomorphous replacement experiments on soaked crystals and a single anomalous dispersion experiment at the selenomethionine f″ peak (Table 1). Data processing was carried out using the hkl suite version 1.98 (*33*). First, the two seleno-

Table 1: Data Collection and Refinement Statistics[a]

| data set | native 1.0 Å X4A | Semet1 1.54 Å rotating anode | Semet2 1.54 Å rotating anode | Semet3 0.997 Å X4A | PtCl4 1 mM 4 h 1.00 Å X4A | IrCl3 10 mM 72 h 1.54 Å rotating anode | IrCl6 10 mM 18 h 1.54 Å rotating anode |
|---|---|---|---|---|---|---|---|
| resolution (Å) | 50−1.55 | 35−2.0 | 35−2.1 | 35−1.8 | 35−1.6 | 35−2.1 | 35−2.8 |
| observations (total) | 249 796 | 79 616 | 176 072 | 206 193 | 393 166 | 68 007 | 32 826 |
| observations (unique) | 30 149 | 13 698 | 12 154 | 19 457 | 52 053 | 12 464 | 5325 |
| $R_{sym}$ (%)[b] | 0.064 | 0.077 | 0.099 | 0.071 | 0.071 | 0.085 | 0.085 |
| | (0.310) | (0.209) | (0.271) | (0.279) | (0.338) | (0.314) | (0.162) |
| completeness (%) | 96.6 | 96.4 | 99.0 | 99.4 | 98.1 | 99.6 | 99.7 |
| | (95.4) | (93.5) | (97.6) | (98.5) | (99.3) | (99.8) | (99.3) |
| $R_{iso}$ (%)[c] | | 8.0 | 8.5 | 8.3 | 20.1 | 10.8 | 18.0 |
| number of sites | | 2 | 2 | 1 | 2 | 1 | 3 |

Refinement: Native Data Set

| | |
|---|---|
| resolution (Å) | 20−1.55 |
| total number of reflections | 28 955 |
| number of total atoms (waters/sulfates) | 1790 (235/6) |
| $R_{cryst}/R_{free}$ (%)[d,e] | 0.228/0.256 |
| rmsd bond length (Å) | 0.007 |
| rmsd bond angle (deg) | 1.39 |
| mean $B$ factor (Å$^2$) | 24.3 |

[a] The values in parentheses are for the highest resolution shell. [b] $R_{sym} = \sum|I_i - \langle I_i\rangle|/\sum\langle I_i\rangle$, where $I_i$ is the observed intensity and $\langle I_i\rangle$ is the average intensity over symmetry-equivalent measurements. [c] $R_{iso} = \sum||F_{PH}| - |F_P||/\sum|F_P|$, where $F_{PH}$ and $F_P$ are the derivative and native structure factors, respectively. [d] $R_{cryst} = \sum||F_{obs}| - |F_{calc}||/\sum|F_{obs}|$, where $F_{obs}$ is the observed and $F_{calc}$ is the calculated structure factors. [e] $R_{free}$ is the $R_{cryst}$ computed from 10% of the reflections that were randomly selected and omitted from the refinement.

methionine sites were located by inspection of isomorphous and anomalous difference Patterson maps. The remaining heavy-metal sites were located using SOLVE (*34*). Inspection of resulting Fourier maps suggested that the hand of the phases needed to be flipped to produce the correct hand. The phases were then improved with RESOLVE (*34*), resulting in a figure of merit of 0.56 for data to 2 Å resolution, and resulting maps to 3.2 Å were of sufficient quality to trace the ART model.

Alternating cycles of model building with O (*35*) and refinement with CNX (*36*) against the selenomet3 data set using a mlhl target resulted in a complete model of the ART protein, excluding the first amino-terminal 12 amino acids and including 235 water molecules and 6 sulfate anions. To refine against the native data, this model was placed by molecular replacement using MOLREP (*37*) and then refined to 1.55 Å resolution against a maximum-likelihood structure factor (mlf) target. A Ramachandron plot calculated in PROCHECK (*38*) reveals no amino acids in the disallowed or generously allowed regions. The coordinates have been deposited in the Protein Data Bank under accession code 2ASK.

*Construction of Mutant ART Molecules.* Mutations R48E, R49E, and R51E and the triple mutant (R48E, R49E, and R51E) were generated by PCR site-directed mutagenesis (Quik Change, Strategene) within the plasmid pCMB098. The following mutant oligonucleotides were used as primers: R48E (5′-TGTTCAGGATCTTGTGAACGTGCACGTTCTCCG-3′), R49E (5′-TCAGGATCTTGTCGTGAAGCACGTTCTCCGCAT-3′), and R51E (5′-TCTTGTCGT CGTGCAGAATCTCCGCATGATCTA-3′), and the presence of the mutation was confirmed by DNA sequencing. The mutants were purified using a scaled-down version of the method described for the purification of wild-type ART. The purified proteins were subjected to cystine mapping by mass spectrometry to confirm that they were folded properly.

*Heparin−Sepharose Chromatography Assay.* Each of the ART variants and wild-type ART was individually subjected to heparin−Sepharose (Amersham-Pharmacia) using similar conditions. Approximately 100 $\mu$g of ART was loaded on 1 mL of resin in binding buffer (5 mM phosphate at pH 6.5/150 mM sodium chloride). The resin was washed with 5 column volumes of binding buffer followed by elution over 20 column volumes using a linear salt gradient from 150 mM to 1 M sodium chloride. ART was monitored by UV absorbance at 280 nm.

*Heparin Enzyme-Linked Immunosorbent Assay (ELISA).* The 96-well plates were coated with 0.2 $\mu$g (100 $\mu$L/well in PBS) anti-ART monoclonal antibody (P3B3), incubated at room temperature, and washed 3 times with TBST (50 mM Tris-HCl at pH 7.5, 0.15 M sodium chloride, and 0.1% Triton X-100). The plate was blocked with a 1× Casein solution (Pierce) for 60 min at room temperature, followed by three TBST washes. During the blocking step, a solution of 20 ng/mL wild-type or mutant ART in TBST with 0.05% BSA as a carrier was prepared. In addition, a 1:10 dilution series of biotin−heparin (Celsus laboratories; BH0323 is a mixture with an average molecular weight of 5 kDa) starting from 2 mg/mL was made, and 5 $\mu$L of each concentration was mixed with 45 $\mu$L of each of the diluted ART solutions (20 ng/mL) in separate tubes, followed by a 1 h room-temperature incubation. After this incubation, 90 $\mu$L of PBST was added to each well along with 10 $\mu$L of the ART/biotin−heparin mixture and incubated at room temperature for 1 h. The plates were then washed with TBST 3 times for 30 s each wash. A 1:8000 dilution of streptavidin−HRP (Southern Biotech) was prepared in PBST (PBS with 0.1% Triton X-100), and 100 $\mu$L of this solution was added to each well and incubated at room temperature for 30 min. Again, the wells were washed with four 30 s TBST washes. The

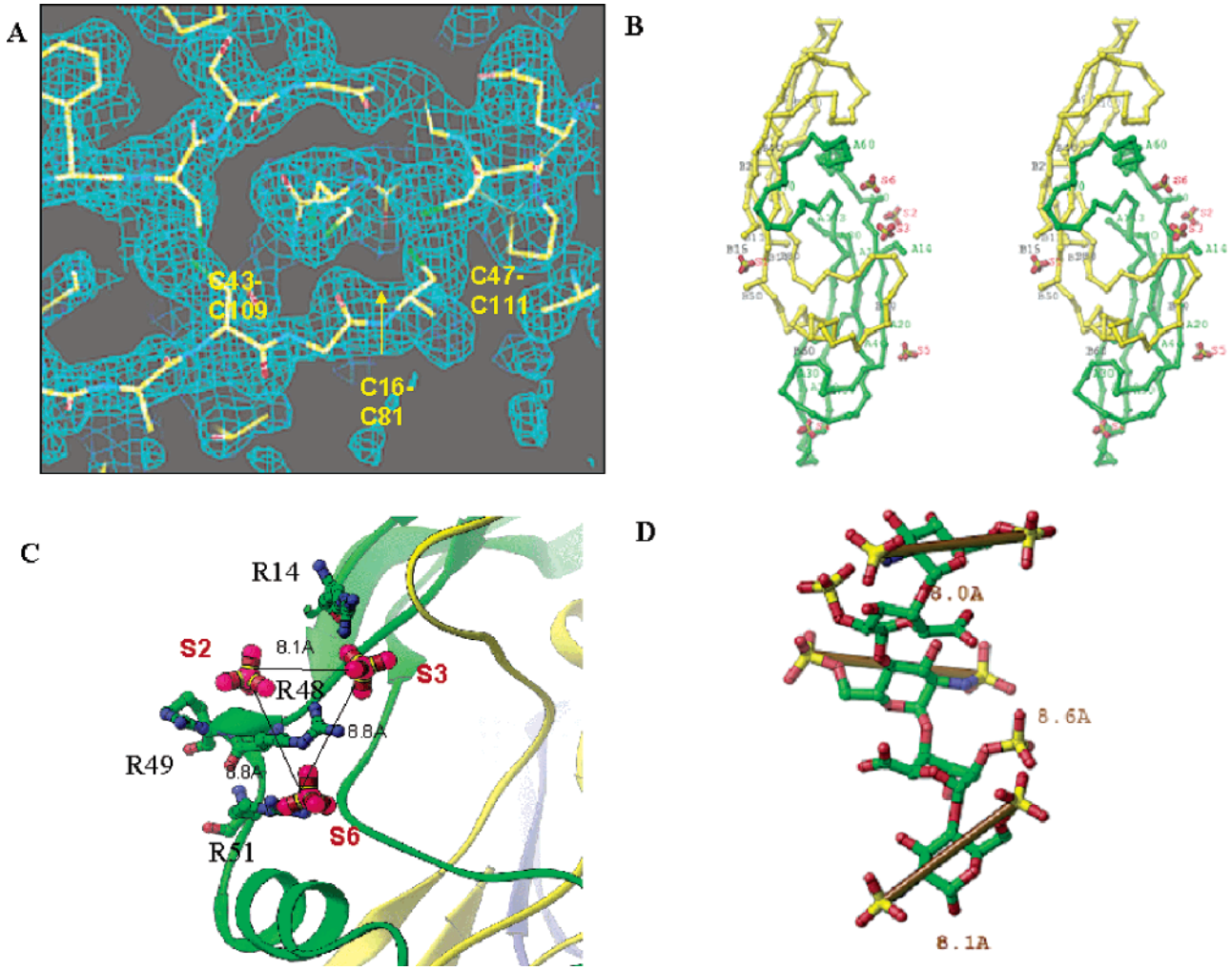


FIGURE 1: Structure and properties of the ART covalent dimer. (A) Representative portion of a $2F_o - F_c$ electron-density map of ART. The map is contoured at 1.2$\sigma$, and the model is the final refined model. (B) Stereoview of the α-carbon trace of the ART covalent dimer (green and yellow chains). Every 10th carbon is labeled. The sulfates are labeled and represented by red and yellow sticks. (C) Molecular interactions of the three sulfates of the cluster which may mimic heparan sulfate with the arginine/side chains of ART. (D) Measurement of the distance between sulfates within single saccharide units in heparin from the structure of FGF1 complexed to FGFR2 and heparin (PDB 1E0O; *40*).

detection substrate was prepared by mixing equal parts of SuperSignal Luminol/Enhancer solution with stable peroxide solution (Pierce). A total of 100 $\mu$L of the substrate was added to each well and incubated for 1 min in the dark with gentle shaking. Light emission was measured using an ABI Tropix luminometer.

*Kinase Receptor Activation* (*KIRA*) *ELISA.* ART activity was determined by its ability to stimulate cRET phosphorylation in NB41A3-mRL3 cells, an adherent murine neuroblastoma cell line that expresses cRET and GFRα3. The KIRA was performed as described (*23*), except that, for the experiments performed in the presence of heparin, the cells were incubated with 250 $\mu$g/mL sodium heparin (Celsus laboratories, PH-0300 mixture with an average molecular weight of approximately 12.5 kDa) prior to stimulation by the ART or an ART variant.

## RESULTS

The structure of human ART was solved using a recombinant form of the protein with 113 amino acids (ART113) expressed in *E. coli* (*39*). To prepare ART for crystallization, the protein was refolded, purified, and concentrated in the presence of a buffer containing high L-arginine concentrations. Crystals were formed only in the presence of sulfate anions. To solve the structure, we attempted molecular replacement with standard programs (Amore/CNX 6D searches). This method failed using either the monomeric or dimeric GDNF or an ART homology model based on the GDNF structure as a search probe. Instead, phases sufficient for clear density interpretation were obtained by combining data collected from several multiple isomorphous replacement experiments with data from a single anomalous dispersion experiment on a crystal of selenomethionine-incorporated ART (Table 1). The model was converted to the native unit cell by molecular replacement and then refined against the native data set to 1.55 Å resolution. A single covalent dimer was observed in the asymmetric unit. The amino-terminal 12 residues are disordered in each monomer; both monomers start at residue 13. There are six sulfate anions modeled in the electron density with temperature factors that are generally higher than the average *B* factor of the protein atoms (24.3 Å$^2$): S1, 24.1; S2, 43.7; S3, 34.2; S4, 32.4; S5, 21.0; and S6, 24.1 Å$^2$.

The ART dimer is in the shape of a letter S, in which sulfate anions decorate the central positively charged region and one of the branches of the S-shaped structure. The ART

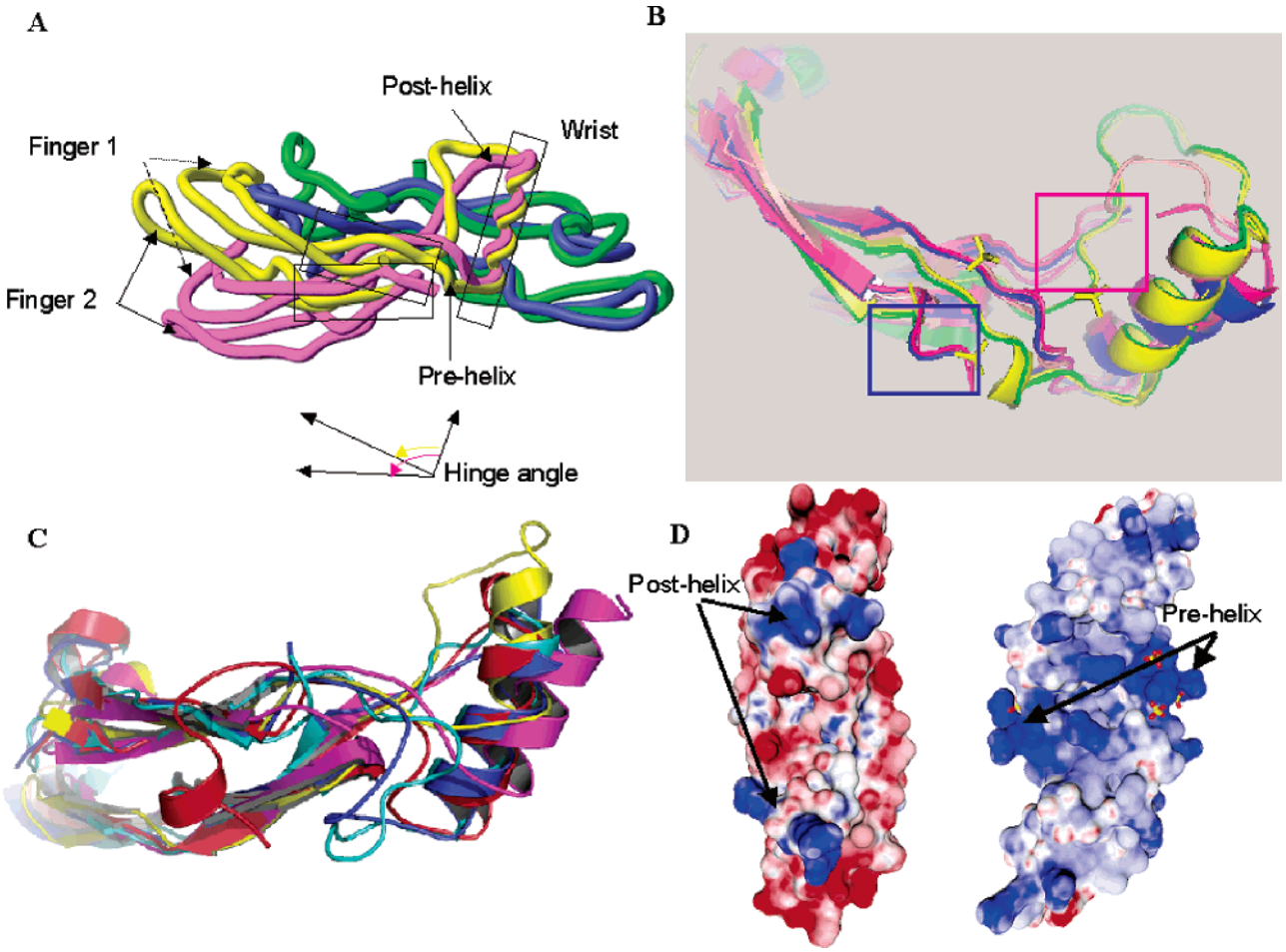


FIGURE 2: Differences between ART and GDNF. (A) Toothpaste representation of the ART dimer superimposed on a GDNF dimer. The ART dimer (yellow and green) and the GDNF dimer 1 (pink and blue) are superimposed by overlaying the helices of monomer 1 of each dimer. (B) Superposition of the two ART monomers and four GDNF monomers by superimposing the two $\beta$-strand-containing fingers. The structure of each ART monomer (yellow and green) significantly differs from each GDNF monomer (purple and blue, red and pink) in pre-helix region (blue box) and post-helix (pink box) regions, causing a rotation of the helix. The post-helix region of one of the GDNF dimers in the asymmetric unit is partially disordered. The pre-helix region is bound by a sulfate cluster in the ART structure (yellow structures near the blue box). (C) Superposition of the "fingers" of the monomers of representative proteins in the cystine knot superfamily, indicating differences in the hinge between "fingers" and "wrists": ART (2ASK; yellow), GDNF (1AGQ; magenta), Tgf-$\beta$2 (1TFG; red), BMP-2 (1REU; dark blue), and OP-1 or BMP-7 (1BMP; cyan). (D) Electrostatic charge distribution of one of the GDNF dimers (left panel) highlighting the positive charge in the post-helix region compared to the electrostatic charge distribution in the pre-helix of the ART dimer (right panel). Relative to the orientation of the proteins in A, GDNF is viewed from the top and ART is viewed from the bottom. Both proteins are contoured at the same potential ranges. The positive charge is blue, and the negative charge is red. Sulfates in ART are denoted with red and yellow sticks.

dimer is covalently linked through Cys 80. Each of the ART monomers is organized by three-disulfide bonds that define the characteristic cystine knot of TGF-$\beta$ superfamily members (Figure 1A). Six sulfate ions with appropriate tetrahedral geometry have been modeled in the ART electron density (Figure 1B); three sulfates clustered together may partly mimic the binding mode of heparan sulfate. The sulfates are separated by approximately 8−9 Å and are arranged at the vertices of an approximate equilateral triangle (Figure 1C). They are tethered to the protein by three positively charged arginine residues from the pre-helix region and a fourth arginine near the amino terminus (Arg 14). A single pivotal residue, Arg 48, interacts with all three sulfates in this cluster (S2, S6, and S3). Its backbone amide hydrogen bonds with sulfate S2, while its side chain forms a bifurcated hydrogen bond between sulfates S6 and S3 (Figure 1C). Additional residues within the helix (Arg 49, Arg 51, and Ser 46) and elsewhere (Arg 14, Ser 73, and carbonyl 72) provide supplementary interactions with each individual sulfate. Sulfate S3 is bound by the side chains of R48 and R14; sulfate S6 is bound by the side chains of R48 and R51; and sulfate S2 is bound by the side chain of R49. The remaining sulfates are not clustered together (Figure 1B); therefore, it remains unclear whether they could also mimic heparan sulfate.

While the overall fold of the ART covalent homodimer is similar to GDNF (*16*), the shape and possibly flexibility of the elongated homodimer differs. Unlike GDNF, ordered segments in the pre-helix and post-helix regions of ART appear to increase the hinge angle between the "fingers" and "wrist" of each monomer (parts A and B of Figure 2). The hinge angle is influenced by the sequence composition in the post-helix and pre-helix regions. The post-helix loop of ART contains a triple proline insertion that is absent in other GFLs (Figure 3). GDNF has a positively charged post-helix loop that is disordered in one of the two homodimers contained within the asymmetric unit (*16*). The pre-helix region of ART contains a positively charged heparin

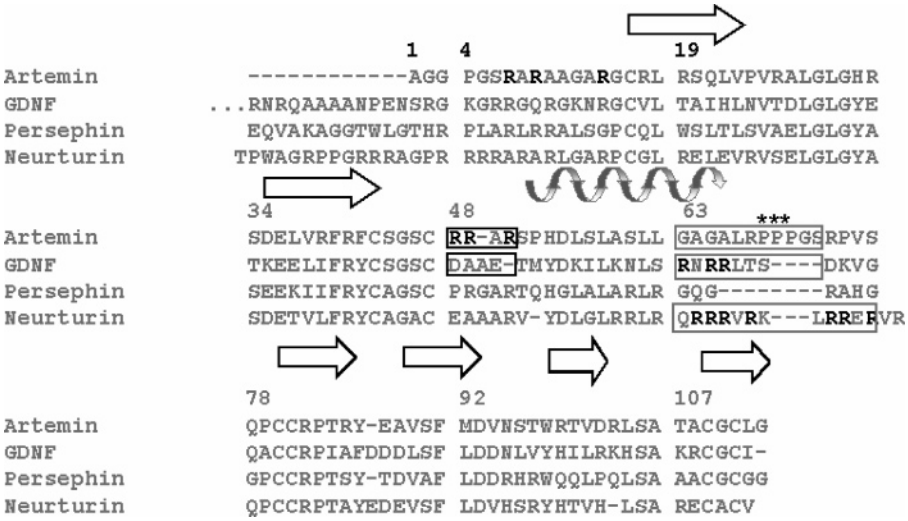


FIGURE 3: Sequence alignment of the human GFL members. The secondary-structural elements within the ART structure are identified above the sequence by designations for α helices (coil) and $\beta$ strands (arrows). The ART residues interacting with sulfates and the residues predicted to comprise the expanded heparan-sulfate-binding site (including Arg14) are black. Residues in the pre-helix region are identified by black boxes, and residues in the post-helix region are identified by gray boxes. The ART proline insertion is indicated by asterisks.

consensus sequence XBBXBX, where B is a basic residue and X is a hydropathic residue (*40*), and is observed to bind sulfates (see results below), while the pre-helix region of GDNF is negatively charged.

One result of this change in the hinge angle within the monomer is that the shape of the ART homodimer differs from that of GDNF (Figure 2A). We measured the hinge angle for available proteins in the TGF-$\beta$ superfamily by calculating the angle between the helical axis and a line drawn perpendicular to the disulfide bonds of the cystine knot. This angle is 83° in ART, approximately 90° in each of the two independent GDNF molecules, and greater than 90° for TGF-$\beta$2 or OP-1 (Figure 2C). This observation is not surprising because these proteins bind different receptors and co-receptors. The hinge angle could impart different co-receptor specificities by altering receptor interactions that occur through the tips of their "fingers".

The enhanced curvature of each ART monomer increases the buried surface area of the ART dimer compared to GDNF. Each ART monomer buries approximately 1093 Å$^2$ of the surface area at the dimer interface, while each GDNF monomer buries only 899 Å$^2$ for the first dimer and 874 Å$^2$ for the second dimer in the asymmetric unit. The difference in the hinge angle explains why molecular replacement with standard programs using the GDNF monomers or dimers as search probes failed to identify the correct structural solution.

ART also differs from GDNF in its overall charge and electrostatic distribution. The calculated pI of human ART is 11.3, while the pI of human GDNF is approximately 8. This difference is reflected in the distribution of local positively charged clusters. GDNF displays a highly localized positive charge centered at the post-helix region with negatively charged amino acids at its finger tips (Figure 2D) (*16*). In contrast, ART is more positively charged, and the charge is scattered more ubiquitously (Figure 2D). In ART, three of the four residues preceding the helix are arginines. GDNF contains two negatively charged residues in this pre-helix region (Figure 3).

The three-sulfate cluster has characteristics that suggest the sulfates mimic the binding mode of heparan sulfate. From the crystal structure of the FGF1/FGFR2/heparin ternary complex, the sulfates within a saccharide-repeating unit of heparin are separated by 8−8.8 Å (*41*) (Figure 1D). These measurements closely match the distance between sulfates S3 and S6 (8.8 Å), sulfates S2 and S6 (8.8 Å), and sulfates S3 and S2 (8.1 Å). We reasoned that the mutation of pre-helix arginines (Arg 48, Arg 49, and Arg 51) or deletion of amino-terminal sequences to remove side chains that contact the sulfate cluster should reduce heparan sulfate binding and that these variants can be used to address a possible role for heparan sulfate in ART signaling.

A sequence alignment of mammalian ART orthologues shows that, while the pre-helix and amino-terminal arginines are highly conserved, arginines that are in the finger-tip regions of human ART are not conserved (Figure 4A). To probe the role of scattered positively charged residues of human ART113 in forming an extended heparin-binding site, we compared human and rat ART113 in heparin binding. The calculated pI of rat ART is 10.0, while human ART has a pI of 11.3. A homology model of rat ART based on the human ART structure indicates that the positive charge distribution of human ART and rat ART is similar in the groove between the two pre-helix regions of the monomer. Rat ART is less positively charged at its finger tips (Figure 4B). However, when we compared the binding affinity of full-length human ART to that of full-length rat ART in a heparin-based ELISA, we observed no measurable difference in their affinities for heparin (data not shown), suggesting that the charge on the human ART finger tips is not required for heparin binding. We then tested the effect of removing the first nine amino-terminal residues of human ART on heparin binding. The truncated form demonstrated a <10-fold reduction in binding affinity (data not shown), indicating that, although unstructured, this region partly contributes to heparin binding. However, the pre-helix region of ART, which is observed to bind sulfates and exhibit high-sequence conservation, may play a more central role in forming the heparin-binding site.

To determine if the pre-helix region may be part of a heparin-binding site, we separately converted to glutamate

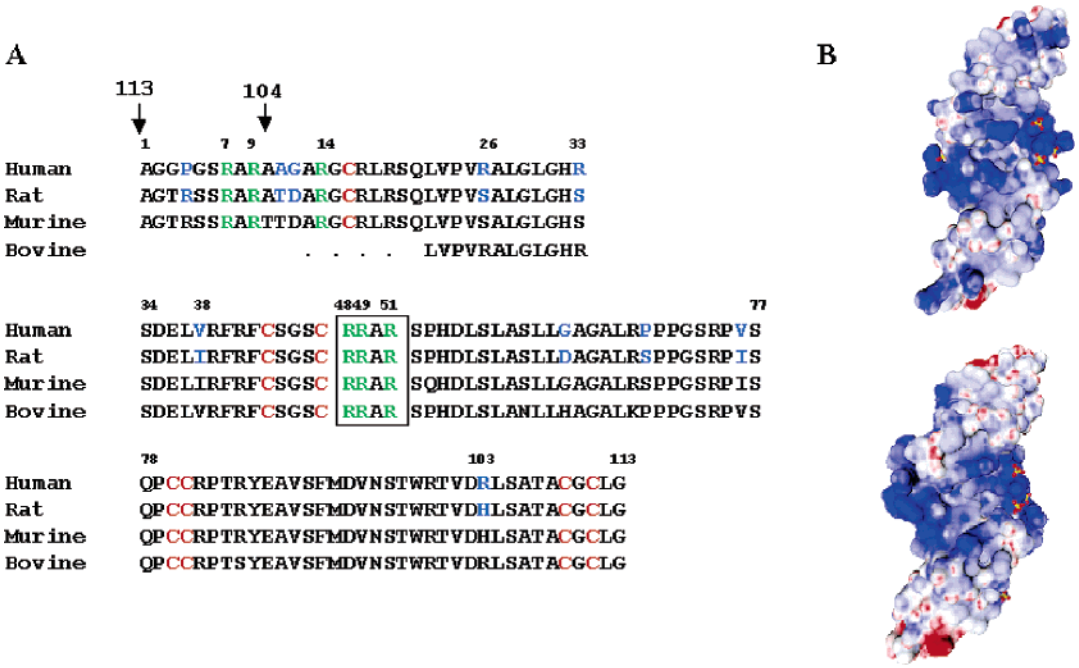


FIGURE 4: Pre-helix-region near the center of the ART dimer is conserved among ART orthologues. (A) Sequence alignment human ART (gi|16950643), rat ART (gi|61097943), bovine ART (gi|61817271), and mouse ART (gi|6753124). Conserved cysteines are highlighted in red. Arginines shown to bind heparin in this study are highlighted in green. Differences between the human and rat ART are highlighted in blue. (B) Structure-based homology model of rat ART (lower panel) compared to the human ART structure (upper panel) colored by electrostatic potential (as in Figure 2D). The sulfates are included in the rat ART model for reference. The heparin binding motif containing residues Art 48, Art 49 and Arg 51 is boxed.

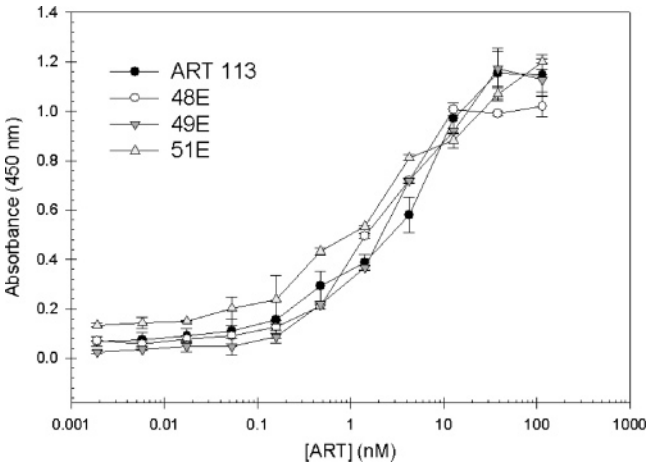


FIGURE 5: ART single-site variants demonstrate similar signaling activity to wild-type human ART. Full-length wild-type ART113 (●), ART-R48E (○), ART-R49E (gray), and ART-R51E (△) all have similar signaling activity in a KIRA assay.

three of the four arginine residues (Arg 48, Arg 49, and Arg 51) in this region that binds sulfate. The ART-R48E, ART-R49E, and ART-R51E variants retained activity in a cRET phosphorylation assay (KIRA), demonstrating that they were properly folded. Wild-type ART and all three Arg to Glu mutants similarly elicited a dose-dependent response with an EC50 averaging about 2.5 nM (Figure 5).

The variants were tested for their ability to bind heparin by retention to a heparin-based resin (Figure 6). Mutation of the pivotal Arg 48 side chain to Glu showed the largest reduction in heparin binding. Upon heparin−Sepharose, wild-type ART113 is the tightest binder (eluting from heparin−Sepharose at 89 mS/cm) and ART-R48E is the weakest binder (eluting at 68 mS/cm), while ART-R49E and ART-R51E bind with an intermediate strength (eluting at 77 and 73 mS/cm, respectively) (Table 2).

To demonstrate that this difference in retention was the result of specific binding to heparin, rather than a nonspecific charge interaction effect with sulfates, the same mutants were tested for retention on a strong cation-exchange resin (HiTrap SP−Sepharose). While SP−Sepharose contains sulfate groups, their distribution differs from those contained within heparin. The difference in salt elution between each mutant and wild-type ART was not as great on SP−Sepharose as on heparin−Sepharose (data not shown). This suggests that heparin forms specific interactions with the variant molecules that cannot be replicated by the SP−Sepharose resin, which harbors a different distribution of negative charges.

The reduced binding affinity of each single-site mutant for heparin was confirmed using an ELISA-based heparin-binding assay. In this assay, 5 kDa biotinylated heparin is bound to ART, captured on a 96-well plate using an ART-specific monoclonal antibody, and detected with streptavidin−HRP and a chemiluminescent substrate (Figure 7A). As shown with heparin−Sepharose binding, ART-R48E exhibited the poorest binding to biotinylated heparin (~30 nM) compared to wild-type ART (~0.5 nM) or either of the other single-site mutants (ART-R49E, 2.5 nM; ART-R51E, 3.0 nM). These data again suggest that the pre-helix region of ART is capable of specifically binding heparan sulfate and that alteration of this site can reduce the affinity by an order of magnitude.

We also tested whether the reduced heparin-binding ART variants would respond differently compared to the wild type in an activity assay measuring a heparin-dependent stimulation of cRET phosphorylation. The activity of wild-type ART is stimulated upon preincubation of cells with exogenous 12.5 kDa heparin (Figure 7B). All three Arg to Glu variants

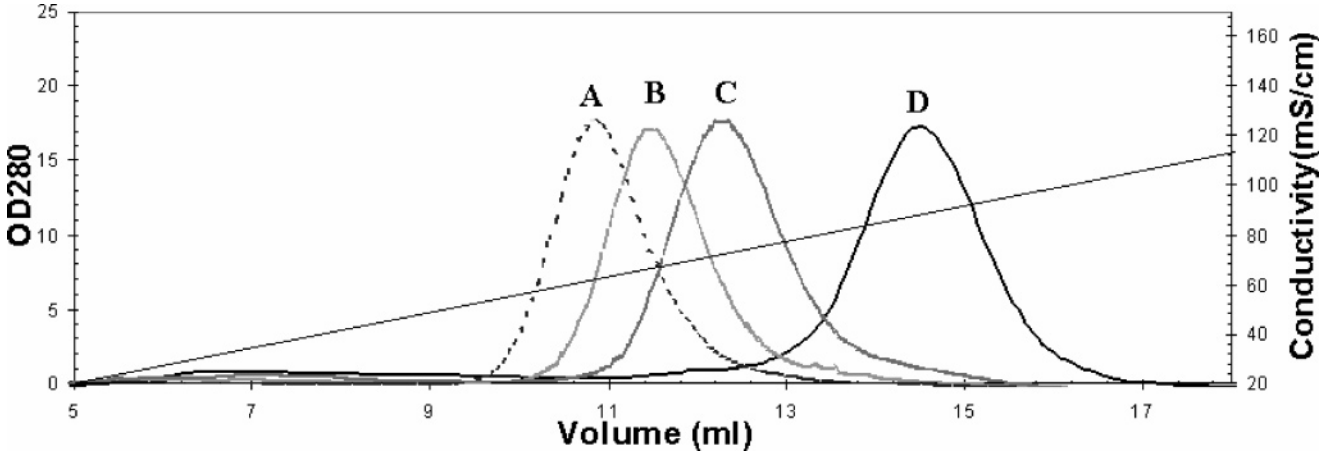


FIGURE 6: ART variants display different heparin-specific chromatic retention profiles. Elution profile of ART variants from a heparin−Sepharose column. The elution peak of wild-type ART113 (D) is compared to that of ART-R48E (A), ART-R49E (C), and ART-R51E (B).

Table 2: Comparison of ART Variants in Heparin Binding and KIRA Assays[a]

| ART form | EC50 heparin binding (nM) | Heparin−Sepharose elution conductivity (mS/cm) | KIRA EC50 without heparin (nM) | KIRA EC50 with heparin (nM) | KIRA ΔEC50 |
|---|---|---|---|---|---|
| ART 113 | 0.5 | 88.9 | 3.5 | 0.5 | 7 |
| 48E | 30.0 | 68.0 | 2.0 | 0.5 | 4 |
| 49E | 2.5 | 77.0 | 3.0 | 0.5 | 6 |
| 51E | 3.0 | 72.5 | 2.0 | 0.4 | 5 |
| 48,49,51E | 5000.0 | 57.0 | 0.8 | 0.8 | 1 |

[a] The KIRA ΔEC50 describes the fold improvement in cRET activation upon the addition of heparin.

similarly demonstrate enhanced activity upon heparin preincubation, as represented by ART-R48E (Figure 7B). These studies suggest that the effect of mutating one amino acid on an extensive heparin-binding surface of the molecule is too minor to trigger an effect on the signaling cascade.

To further pursue this hypothesis, we constructed an ART variant containing all three mutations (ART-R48E,R49E, R51E) to determine the cumulative effect of these mutations upon heparin binding. We measured its affinity for heparin and its activity in the heparin-dependent stimulation of the cRET phosphorylation assay. The triple mutant bound biotinylated heparin with at least 3 orders of magnitude lower affinity than the wild type and 2 orders of magnitude lower affinity compared to the single ART-R48E mutation (Figure 8A and Table 2). It binds to heparin−Sepharose more weakly than the single-site mutants, eluting at 57 mS/cm. Even in the absence of exogenous heparin, the triple mutant displayed an improved EC50 value for cRET activation compared to wild-type ART (EC50 of 0.8 nM rather than 3.5 nM; Table 2). In the presence of heparin, the triple mutant does not demonstrate any heparin-dependent stimulation of activity as had been observed for wild-type ART (Figure 8B). These studies show that the extensive heparin-binding surface of the molecule can be altered by the triple mutant and point to the central groove of ART as a crucial region of heparin binding.

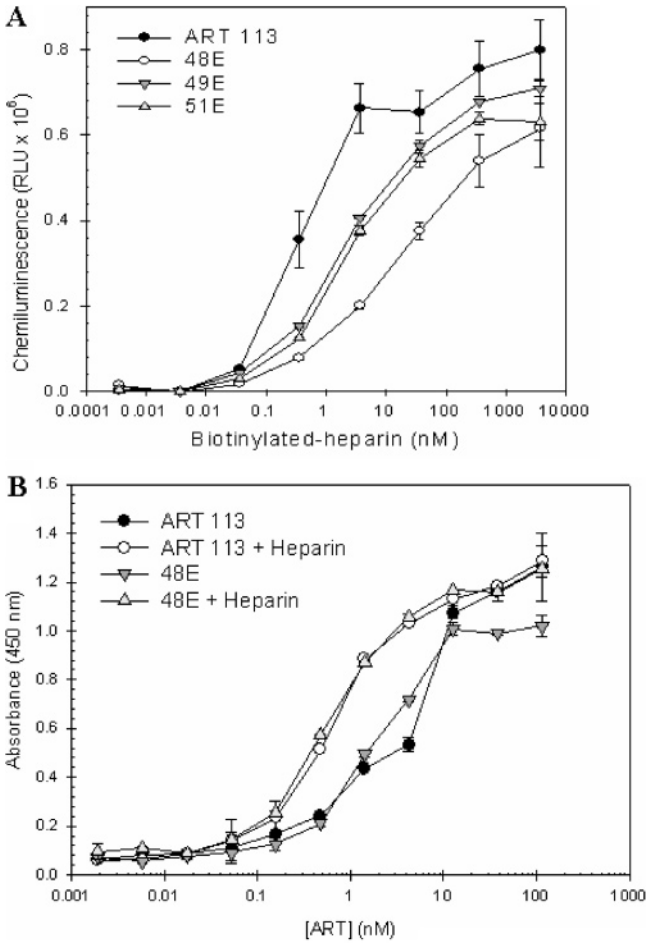


FIGURE 7: Behavior of single-site variants relative to wild-type ART in heparin-binding and heparin-dependent stimulation of cRET phosphorylation. (A) Heparin ELISA for wild-type ART113 (●) and each ART single-site variant: R48E (○), R49E (gray), and R51E (△). Each sample was analyzed in triplicate. Error bars denote the standard error of the mean (SEM). (B) Stimulation of signaling activity by ART-R48E upon the addition of heparin. KIRA of wild-type ART113 in the absence (●) and presence (○) of 250 $\mu$g/mL heparin compared to ART-R48E in the absence (gray) and presence (△) of 250 $\mu$g/mL heparin. Similar curves to ART-R48E were observed for ART-R49E and ART-R51E.

## DISCUSSION

Heparin binding has a profound effect on the pharmacokinetic and pharmacodynamic properties of proteins such as HGF/SF (*42*), which was the basis for our investigation of whether the heparin-binding site could be identified and re-engineered. In solving the structure of human ART, we

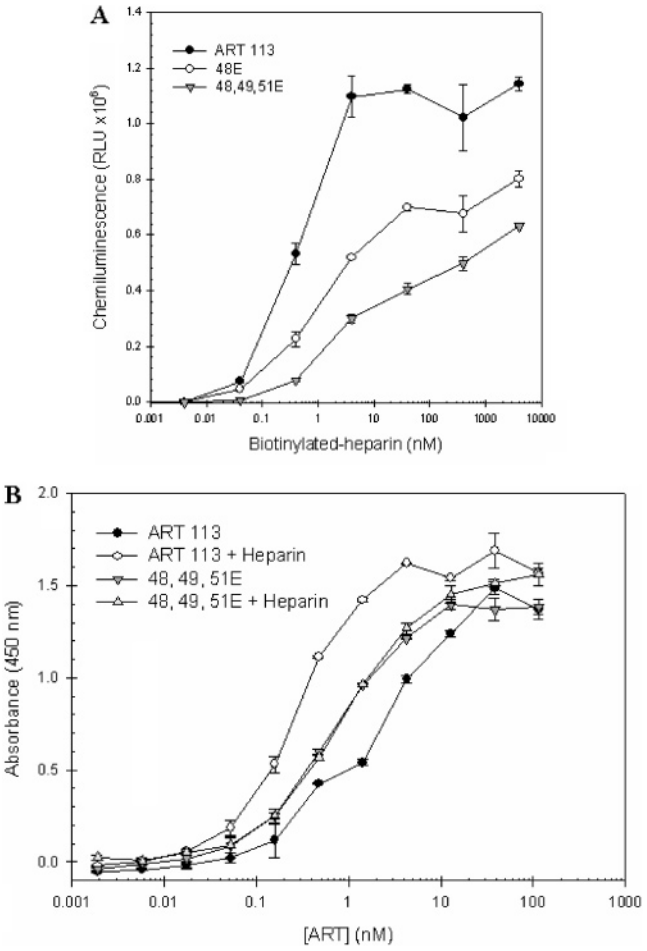


FIGURE 8: Behavior of triple-mutant ART relative to the wild type in heparin-binding and heparin-dependent stimulation of cRET phosphorylation. (A) Heparin ELISA with biotinylated 5 kDa heparin for wild-type ART113 (●), ART-R48E (○), and ART-R48E,R49E,R51E (gray). Each sample was analyzed in triplicate. Error bars denote the SEM. (B) Stimulation of signaling activity by the ART triple mutant upon the addition of heparin compared to that of wild-type ART. KIRA of wild-type ART113 in the absence (●) and presence (○) of 250 $\mu$g/mL heparin compared to ART-R48E,R49E,R51E in the absence (gray) and presence (△) of 250 $\mu$g/mL heparin.

observed a triad of bound sulfate ions that resembled the spacing of sulfates within heparin and identified this region as a putative heparin-binding site. To test if ART is a heparin-binding protein, we generated point mutations at each of these sulfate-binding residues, expressed the proteins, and characterized the effects of the mutations in heparin-binding assays using soluble and immobilized heparin. We demonstrate that ART is a heparin-binding protein and localize the key residues for heparin binding within the pre-helix region of ART.

GFLs have predicted heparin-binding site(s) in different regions of their sequences that would result in their placement on different locations along the surface of the molecule (Figures 2D and 3). Within the two sequence stretches between the "wrist" and "fingers", ART has a putative heparin-binding site (C**RR**A**R**S) in its pre-helix region, while GDNF (S**RS**R**R**L) and NTN (**RR**V**R**KL**RR**E**R**) have putative heparin-binding sites in their post-helix loops. This places the heparin-binding sites on opposite sides of the structure. PSP, on the other hand, has no obvious heparin-binding sites in the hinge (Figure 3). The locations and strengths of these heparin-binding clusters may have different functional consequences on the role of heparin binding to these cytokines both in vivo and in cell-based assays.

Sequence comparisons of ART orthologues demonstrate that the amino-terminal and pre-helix arginines are highly conserved and thus could represent a conserved HSPG-binding function. The two sulfate-decorated pre-helix regions of each human ART dimer are connected by a positively charged central groove that is appropriate in dimension to bind heparin sulfate oligosaccharides. Human ART, in contrast to rat ART, has positive charges scattered throughout its finger regions that are not conserved (Figure 4B). These charge differences do not effect heparin binding. This observation, along with the identification of bound sulfate ions in the ART pre-helix region, suggests that heparin binding is localized to a specific region and not because of a general electrostatic effect.

Although the amino terminus was not detected in our ART structure, we tested its contribution in heparin binding by proteolytically generating a truncated variant (ART104) with residues 1−9 removed and measuring its ability to bind heparin relative to the full-length ART113. The truncation variant has a 10-fold lower affinity for heparin (data not shown), suggesting that the amino terminus may also form part of the heparin-binding site. The amino terminus is likely to be in close proximity to the pre-helix region and to the positively charged groove, because the amino-terminal Arg14 contributes to sulfate ion binding in conjunction with the arginines identified in the pre-helix region (Figure 1C). NTN and PSP also have positively charged amino-terminal sequences, **RRR**AGP**RRRR**A**R** and **R**L**RR**, respectively (Figure 3), that may also act as heparan-sulfate-binding regions.

The heparin-binding variants provide a tool to determine whether the heparin-binding and/or signaling activity of ART can be modulated. All three single-point mutations reduced 5 kDa heparin affinity and decreased retention on heparin−Sepharose, and the triple mutant showed the greatest decrease in affinity (Table 2). Interestingly, among the single-site mutants, the magnitude of reduction in heparin affinity correlates with the location and number of interactions that each Arg makes with the sulfates in the structure. Arg 48 is located in the center of the sulfate triangle, and its side chain interacts with sulfates S3 and S6, while Arg 49 and Arg 51 are located on the periphery of the sulfate triangle and each makes only one salt bridge to a single sulfate ion. The R48E mutation produced the largest reduction in heparin binding, which is consistent with its central structural role.

While the 5 kDa heparin mixture, used in the heparin ELISA, was ideally suited to probe subtle binding effects of the single-point mutations in ART, a 12.5 kDa heparin mixture, more closely resembling the long GAG chains found in vivo, was used in the receptor activation assay. Given the large amount and size of heparan sulfate on the cell surface in the form of HSPGs, 5 kDa heparin was considered ill-suited to test the effect of heparin binding to the mutants in the cRET activation assay and 12.5 kDa heparin was used.

The addition of 12.5 kDa heparin resulted in a similar cRET activity enhancement for either wild-type ART or each of the three ART single-site mutants but resulted in no enhancement for the triple mutant. The triple mutant

demonstrated enhanced cRET activation over wild-type ART in the absence of heparin. One hypothesis for the lack of response of the single-site mutations relative to the wild type is that their modifications were not sufficiently potent or extensive to produce effects on heparin binding that could be detected in the cell-signaling assay. Unlike a single-site mutation, the triple mutation appears to partly mimic heparin binding to wild-type ART by increasing the potency of cRET activation and preventing exogenous heparin from binding and further stimulating activity to the extent observed for the single-point mutants or wild-type ART. These data support the hypothesis that Arg 48, Arg 49, and Arg 51 contained within the pre-helix region of ART may play a role in heparin binding.

ART may have a different response to specific cell-surface-bound HSPGs in vivo than to soluble heparin added ex vivo. Heparin and heparan sulfate are not identical. There are subtle differences in their saccharide sequences. Heparan sulfate is composed of more varied saccharide units. Heparin is more substituted with sulfo groups. While heparin has an average of 2.7 negative charges per disaccharide, there are fewer than 2 negative charges for heparan sulfate (*43*). The amino acids R48, R49, and R51 may contribute more significantly toward binding the highly sulfonated heparin than in binding the protein-bound heparan sulfate. Many growth factors, such as basic fibroblast growth factor (bFGF), have been shown to be specific for only a small subset of the diverse array of heparan sulfate variants (*44*).

The enhancement in cRET activation upon the addition of exogenous heparin to the ART-signaling assay contrasts with studies by Barnett and co-workers or Davies and co-workers, who observed that the addition of exogenous heparan sulfate or heparin to either Madin−Darby canine kidney or PC-12 rat adrenal medullary phaeochromocytoma cells inhibits GDNF signaling (*29*, *45*). Their explanation was that the exogenous GAG prevented the HSPGs at the cell surface from binding GDNF and recruiting GDNF to the cell membrane. The discrepancy between those studies and ours is partly reconcilable by identification of differences between the two systems. GDNF and ART have distinct co-receptors and form distinct signaling complexes. In the absence of heparin, the affinity of ART for GFRα3/cRET is significantly lower than the affinity of GDNF for GFRα-1/cRET, as measured by their abilities to bind to GFRα1-Ig or GFRα3-Ig immobilized to a Biacore chip surface (*23*). Binding to soluble heparin may increase the avidity of ART or help orient it for proper receptor binding, resulting in an increase in its apparent binding to its receptors. ART is more basic than GDNF and may bind more nonspecifically to cell membranes without the countercharge of heparin. Heparin binding to wild-type ART or construction of the triple R to E mutation may orient ART properly so that it can productively bind to its receptors. Last, as demonstrated here, the pre-helix and post-helix heparin recognition motifs in ART and GDNF map to opposite surfaces (Figure 2D); binding exogenous heparin may interfere with the recruitment function of HSPGs in the GDNF case but not in the ART case. Beyond its potential role in recruiting GFLs to the cell surface, HSPGs may increase the avidity of GFL binding or directly mediate interactions between the GFLs and their receptors. While a heparin-dependent receptor binding activity has been reported for bFGF, HGF, a splice variant of PDGF, heparin-binding epidermal growth factor (EGF), VEGF, and neuregulins, its role in most of these cases is not well-understood (reviewed in ref *44*). Further studies are necessary to specifically address which of these or other possible mechanisms of action are relevant for ART.

We favor a model in which certain syndecans or glypicans are upregulated to direct ART to cellular membranes that contain signaling receptors and orient it in such a way to promote receptor binding. Syndecans, which are the major form of membrane-associated HSPGs on many cells, have been shown to have variable heparan sulfate glycosaminoglycan structures, and the pattern of syndecan expression differs in a cell-specific manner (*46*). The potential to regulate growth factor activity by temporally regulating the expression levels of syndecans is an accepted mechanism of action for other growth factors. Rapid changes in the expression of syndecans have been observed during critical periods of development and correlate with a change in relative expression levels of growth factors bFGF and acidic fibroblast growth factor (aFGF) (*44*).

In summary, we have successfully demonstrated that ART is a heparin-binding protein and employed a rational, structure-based design to reduce heparin binding without compromising biological function. In addition, the crystal structure of ART shows clear differences from GDNF that could account for its selectivity for its specific GFRα co-receptor. The structure−activity studies for ART should be invaluable in designing novel ART-based therapeutics with improved pharmaceutical properties.

## ACKNOWLEDGMENT

We gratefully acknowledge Craig Ogata at the X4C beamline at Brookhaven National Laboratory for help in setting up data collection. We thank Ami Horne for help in constructing the mutant ART clones and Adrian Whitty and Rich Cate for rewarding discussions and a critical reading of the manuscript. The authors declare no financial conflict of interest in publication of this manuscript.

## REFERENCES

1. Baloh, R. H., Tansey, M. G., Lampe, P. A., Fahrner, T. J., Enomoto, H., Simburger, K. S., Leitner, M. L., Araki, T., Johnson, E. M., Jr., and Milbrandt, J. (1998) Artemin, a novel member of the GDNF ligand family, supports peripheral and central neurons and signals through the GFRα3−RET receptor complex, *Neuron 21*, 1291−1302.
2. Rosenblad, C., Gronborg, M., Hansen, C., Blom, N., Meyer, M., Johansen, J., Dago, L., Kirik, D., Patel, U. A., Lundberg, C., Trono, D., Bjorklund, A., and Johansen, T. E. (2000) *In vivo* protection of nigral dopamine neurons by lentiviral gene transfer of the novel GDNF-family member neublastin/artemin, *Mol. Cell Neurosci. 15*, 199−214.
3. Masure, S., Geerts, H., Cik, M., Hoefnagel, E., van den Kieboom, G., Tuytelaars, A., Harris, S., Lesage, A. S., Leysen, J. E., van der Helm, L., Verhasselt, P., Yon, J., and Gordon, R. D. (1999) Enovin, a member of the glial cell-line-derived neurotrophic factor (GDNF) family with growth promoting activity on neuronal cells. Existence and tissue-specific expression of different splice variants, *Eur. J. Biochem. 266*, 892−902.
4. Kotzbauer, P. T., Lampe, P. A., Heuckeroth, R. O., Golden, J. P., Creedon, D. J., Johnson, E. M., Jr., and Milbrandt, J. (1996) Neurturin, a relative of glial-cell-line-derived neurotrophic factor, *Nature 384*, 467−470.
5. Milbrandt, J., de Sauvage, F. J., Fahrner, T. J., Baloh, R. H., Leitner, M. L., Tansey, M. G., Lampe, P. A., Heuckeroth, R. O.,

Kotzbauer, P. T., Simburger, K. S., Golden, J. P., Davies, J. A., Vejsada, R., Kato, A. C., Hynes, M., Sherman, D., Nishimura, M., Wang, L. C., Vandlen, R., Moffat, B., Klein, R. D., Poulsen, K., Gray, C., Garces, A., Johnson, E. M., Jr., et al. (1998) Persephin, a novel neurotrophic factor related to GDNF and neurturin, *Neuron 20*, 245−253.

6. Lin, L. F., Doherty, D. H., Lile, J. D., Bektesh, S., and Collins, F. (1993) GDNF: A glial cell line-derived neurotrophic factor for midbrain dopaminergic neurons, *Science 260*, 1130−1132.
7. Honma, Y., Araki, T., Gianino, S., Bruce, A., Heuckeroth, R. O., Johnson, E. M., and Milbrandt, J. (2002) ART is a vascular-derived neurotrophic factor for developing sympathetic neurons, *Neuron 35*, 267−282.
8. Choi-Lundberg, D. L., and Bohn, M. C. (1995) Ontogeny and distribution of glial cell line-derived neurotrophic factor (GDNF) mRNA in rat, *Brain Res. Dev. Brain Res. 85*, 80−88.
9. Daopin, S., Piez, K. A., Ogawa, Y., and Davies, D. R. (1992) Crystal structure of transforming growth factor-$\beta$2: An unusual fold for the superfamily, *Science 257*, 369−373.
10. Schlunegger, M. P., and Grutter, M. G. (1992) An unusual feature revealed by the crystal structure at 2.2 Å resolution of human transforming growth factor-$\beta$2, *Nature 358*, 430−434.
11. Griffith, D. L., Keck, P. C., Sampath, T. K., Rueger, D. C., and Carlson, W. D. (1996) Three-dimensional structure of recombinant human osteogenic protein 1: Structural paradigm for the transforming growth factor $\beta$ superfamily, *Proc. Nat. Acad. Sci. U.S.A. 93*, 878−883.
12. Scheufler, C., Sebald, W., and Huelsmeyer, M. (1999) Crystal structure of human bone morphogenic protein-2 at 2.7 Å resolution, *J. Mol. Biol. 287*, 103−115.
13. Oefner, C., D'Arcy, A., Winkler, F. K., Eggimann, B., and Hosang, M. (1992) Crystal structure of human platelet-derived growth factor BB, *EMBO J. 11*, 3921−3926.
14. McDonald, N. Q., Lapatto, R., Murray-Rust, J., Gunning, J., Wlodawer, A., and Blundell, T. L. (1991) New protein fold revealed by a 2.3 Å resolution crystal structure of nerve growth factor, *Nature 354*, 411.
15. Muller, Y. A., Christinger, H. W., Keyt, B. A., and deVos, A. M. (1997) The crystal structure of vascular endothelial growth factor (VEGF) refined to 1.93 Å resolution: Multiple copy flexibility and receptor binding, *Structure 5*, 1325.
16. Eigenbrot, C., and Gerber, N. (1997) X-ray structure of glial cell-derived neurotrophic factor at 1.9 Å resolution and implications for receptor binding, *Nat. Struct. Biol. 4*, 435−438.
17. Jing, S., Wen, D., Yu, Y., Host, P. L., Luo, Y., Fang, M., Tamir, R., Antonio, L., Hu, Z., Cupples, R., Louis, J. C., Hu, S., Altrock, B. W., and Fox, G. M. (1996) GDNF-induced activation of the ret protein tyrosine kinase is mediated by GDNFR-$\alpha$, a novel receptor for GDNF, *Cell 85*, 113−1124.
18. Baloh, R. H., Tansey, M. G., Golden, J. P., Creedon, D. J., Heuckeroth, R. O., Keck, C. L., Zimonjic, D. B., Popescu, N. C., Johnson, E. M., Jr., and Milbrandt, J. (1997) TrnR2, a novel receptor that mediates neurturin and GDNF signaling through Ret, *Neuron 18*, 793−802.
19. Jing, S., Yu, Y., Fang, M., Hu, Z., Holst, P. L., Boone, T., Delaney, J., Schultz, H., Zhou, R., and Fox, G. M. (1997) GFR$\alpha$-2 and GFR$\alpha$-3 are two new receptors for ligands of the GDNF family, *J. Biol. Chem. 272*, 33111−33117.
20. Sanicola, M., Hession, C., Worley, D., Carmillo, P., Ehrenfels, C., Walus, L., Robinson, S., Jaworski, G., Wei, H., Tizard, R., Whitty, A., Pepinsky, R. B., and Cate, R. L. (1997) Glial cell line-derived neurotrophic factor-dependent RET activation can be mediated by two different cell-surface accessory proteins, *Proc. Natl. Acad. Sci. U.S.A. 94*, 6238−6243.
21. Nishino, J., Mochida, K., Ohfuji, Y.Shimazaki, T., Meno, C., Ohishi, S., Matsuda, Y., Fujii, H., Saijoh, Y., and Hamada, H. (1999) GFR $\alpha$3, a component of the artemin receptor, is required for migration and survival of the superior cervical ganglion, *Neuron 23*, 725−736.
22. Baloh, R. H., Tansey, M. G., Johnson, E. M., Jr., and Milbrandt, J. (2000) Functional mapping of receptor specificity domains of glial cell line-derived neurotrophic factor (GDNF) family ligands and production of GFR$\alpha$-1 RET-specific agonists, *J. Biol. Chem. 275*, 3412−3420.
23. Carmillo, P, Dago, L., Day, E. S., Worley, D. S., Rossomando, A., Walus, L., Orozco, O., Buckley, C., Miller, S., Tse, A., Cate, R. L., Rosenblad, C., Sah, D. W., Gronborg, M., and Whitty, A. (2005) Glial cell line-derived neurotrophic factor (GDNF) receptor $\alpha$-1 (GFR$\alpha$1) is highly selective for GDNF versus artemin, *Biochemistry 44*, 2545−2554.
24. Eketjäll, S., Fainzilber, M., Murray-Rust, J., and Ibanez, C. F. (1999) Distinct structural elements in GDNF mediate binding to GFR$\alpha$1 and activation of the GFR$\alpha$1−cRET receptor complex, *EMBO J. 18*, 5901−5910.
25. Leppänen, V. M., Bespalov, M. M., Runeberg-Roos, P., Puurand, U., Merits, A., Saarma, M., and Goldman, A. (2004) The structure of GFR$\alpha$1 domain 3 reveals new insights into GDNF binding and RET activation, *EMBO J. 23*, 1452−1462.
26. Hileman, R. E., Fromm, J. R., Weiler, J. M., and Linhardt, R. J. (1998) Glycosaminoglycan−protein interactions: Definition of consensus sites in glycosaminoglycan binding proteins, *Bioessays 20*, 156−167.
27. Rapraeger, A. C., Krufka, A., and Olwin, B. B. (1991) Requirement of heparan sulfate for bFGF-mediated fibroblast growth and myoblast differentiation, *Science 252*, 1705−1708.
28. Lyon, M., Deakin, J. A., Rahmoune, H., Fernig, D. G., Nakamura, T., and Gallagher, J. T. (1998) Hepatocyte growth factor/scatter factor binds with high affinity to dermatan sulfate, *J. Biol. Chem. 273*, 271−278.
29. Barnett, M., W., Fisher, C. E., Perona-Wright G., and Davies, J. A. (2002) Signaling by glial cell line-derived neurotrophic factor (GDNF) requires heparan sulfate glycosaminoglycan, *J. Cell Sci. 115*, 4495−4503.
30. Rickard, S. M., Mummery, R. S., Mulloy, B., and Rider, C. C. (2003) The binding of human glial cell line-derived neurotrophic factor to heparin and heparan sulfate: Importance of 2-O-sulfate groups and effect on its interaction with its receptor, GFR$\alpha$1, *Glycobiology 13*, 419−426.
31. Tanaka, M., Xiao, H., and Kiuchi, K. (2002) Heparin facilitates glial cell line-derived neurotrophic factor signal transduction, *NeuroReport 13*, 1913−1916.
32. Leahy, D. J., Hendrickson, W. A., Aukhil, I., and Erickson, H. P. (1992) Structure of a fibronectin type III domain from tenascin phased by MAD analysis of the selenomethionyl protein, *Science 258*, 987−991.
33. Otwinowski, Z., and Minor, W. (1997) Processing X-ray diffraction data collected in oscillation mode, *Methods Enzymol. 276*, 307−326.
34. Terwilliger, T. C., and Berendzen, J. (1999) Automated MAD and MIR structure solution, *Acta Crystallogr., Sect. D: Biol. Crystallogr. 55* (part 4), 849−861.
35. Jones, T. A., Zou, J. Y., Cowan, S. W., and Kjeldgaard, M. (1991) Improved methods for building protein models in electron density maps and the location of errors in these models, *Acta Crystallogr., Sect. A: Found. Crystallogr. 47* (part 2) 110−119.
36. Brunger, A. T., Adams, P. D., Clore, G. M., DeLano, W. L., Gros, P., Grosse-Kunstleve, R. W., Jiang, J.-S., Kuszewski, J., Nilges, M., Pannu, N. S., Read, R. J., Rice, L. M., Simonson, T., and Warren, G. L. (1998) Crystallography and NMR system: A new software suite for macromolecular structure determination, *Acta Crystallogr., Sect. D: Biol. Crystallogr. 54* (part 5), 905−921.
37. Vagin, A., and Teplyakov, A. (1997) MOLREP: An automated program for molecular replacement, *J. Appl. Crystallogr. 30*, 1022−1025.
38. Laskowski, R. A., MacArthur, M. W., Moss, D. S., and Thornton, J. M. (1993) Procheck: A program to check stereochemical quality of protein structures, *J. Appl. Crystallogr. 26*, 283−290.
39. Gardell, L. R., Wang, R., Ehrenfels, C., Ossipov, M. H., Rossomando, A. J., Miller, S., Buckley, C., Cai, A. K., Tse, A., Foley, S. F., Gong, B., Walus, L., Carmillo, P., Worley, D., Huang, C., Engber, T., Pepinsky, B., Cate, R. L., Vanderah, T. W., Lai, J., Sah, D. W., and Porreca, F. (2003) Multiple actions of systemic ART in experimental neuropathy, *Nat. Med. 9*, 1383−1389.
40. Cardin, A. D., and Weintraub, H. J. (1989) Molecular modeling of protein−glycosaminoglycan interactions, *Arterioscler. Thromb. Vasc. Biol. 9*, 21−32.
41. Pellegrini, L., Burke, D. F., von Delft, F., Mulloy, B., and Blundell, T. L. (2000) Crystal structure of fibroblast growth factor receptor ectodomain bound to ligand and heparin, *Nature 407*, 1029−1034.
42. Hartmann, G., Prospero, T., Brinkmann, V., Ozcelik, O., Winter, G., Hepple, J., Batley S., Bladt, F., Sachs, M., Birchmeier, C.,

Birchmeier, W., and Gherardi, E. (1997) Engineered mutants of HGF/SF with reduced binding to heparan sulphate proteoglycans, decreased clearance and enhanced activity *in vivo*, *Curr. Biol. 8*, 125−134.
43. Muñoz, E. M, and Linhardt, R. J. (2004) Heparin-binding domains in vascular biology, *Arterioscler. Thromb. Vasc. Biol. 24*, 1549−1557.
44. Carey, D. J. (1997) Syndecans: Multifunctional cell-surface co-receptors, *Biochem. J. 327*, 1−16.
45. Davies, J. A., Yates, E. A., and Turnbull, J. E. (2003) Structural determinants of heparan sulphate modulation of GDNF signaling, *Growth Factors 21*, 109−119.
46. Kim, C. W., Goldberger, O. A., Gallow, R. L., and Bernfield, M. (1994) Members of the syndecan family of heparin sulfate proteoglycans are expressed in distinct cell-, tissue- and development-specific patterns, *Mol. Biol. Cell 5*, 797−805.

BI060035X